

Crystal electric field excitation and vibrational properties of the quantum spin liquid candidate LiYbSe₂

Enlai Wang,¹ Min Zhang^{1,*}, Chao An,¹ Ying Zhou,¹ Yonghui Zhou,² Jian Zhou³, and Zhaorong Yang^{1,2,4,†}

¹*Institutes of Physical Science and Information Technology, Anhui University, Hefei 230601, China*

²*Anhui Key Laboratory of Low-Energy Quantum Materials and Devices, High Magnetic Field Laboratory, HFIPS, Chinese Academy of Sciences, Hefei 230031, China*

³*National Laboratory of Solid State Microstructures & Department of Materials Science and Engineering, Nanjing University, Nanjing 210093, China*

⁴*Collaborative Innovation Center of Advanced Microstructures, Nanjing 210093, China*

 (Received 20 December 2023; revised 29 March 2024; accepted 15 April 2024; published 1 May 2024)

LiYbSe₂ was recently discovered and assumed to be a new member of the quantum spin liquid candidates. In the paper, polarization-resolved Raman scattering and temperature-dependent Raman scattering experiments were utilized to study the elementary excitations in LiYbSe₂. Four phonon modes with E_g , T_{2g}^1 , T_{2g}^2 , and A_{1g} symmetry, respectively, and three crystal electric field (CEF) excitations, including CEF1, CEF2, and CEF3 at 116.2, 200.9, and 232.1 cm⁻¹, respectively, were conclusively identified. With 633 and 532 nm excitation, resonant conditions were satisfied and caused the breakdown of selection rules for T_{2g} and also prompted the observation of higher-order modes. Helicity-resolved CEF modes were studied based on circularly polarized light and the conservation law of angular momentum. Moreover, CEF modes showed abnormal redshift with decreasing temperature which can be attributed to the reduction of electronegativity of Se atoms due to the lattice contraction. Contributing to the close energy between E_g and CEF1, weak CEF-phonon coupling was induced in this system and caused abnormal softening of E_g at low temperature. The CEF excitations and vibration properties studied here provide information about the electronic elementary excitations, which help to further study or control the frustrated magnetism and novel quantum spin liquid state in LiYbSe₂.

DOI: [10.1103/PhysRevB.109.174101](https://doi.org/10.1103/PhysRevB.109.174101)

I. INTRODUCTION

In frustrated magnets, the competing exchange interactions cannot be simultaneously satisfied, resulting in some systems with a large degeneracy of the ground state [1]. One of the fascinating ultimate ground states is quantum spin liquid (QSL), in which quantum fluctuation is rather strong to prevent conventional spin order even at 0 K and some exotic quantum magnetisms are introduced [1–3]. The research on QSL materials initially focused on the spin- $\frac{1}{2}$ systems such as Cu²⁺ based compounds [4,5]. Nowadays, the family of QSL candidates has been extended to rare-earth systems, in which the combination of spin-orbit coupling (SOC) and crystal electric field (CEF) results in a ground state of Kramers doublet, leading to an effective spin- $\frac{1}{2}$ description that strongly enhances quantum fluctuations and then promotes the QSL ground state [6–10]. In addition, the CEF strongly affects the ground state that defines properties of magnetism, conductivity, etc. [11]; meanwhile, interactions between CEF and other excitations may lead to energy shift, or emergent functionalities, e.g., the superconductivity mediated by the coupling between CEF and electron-hole pairs in UPd₂Al₃ [12].

Recently, a large family of alkali-metal rare-earth chalcogenides $AReCh_2$ (A = alkali metal, Re = rare earth, Ch = O, S, Se) has attracted intense attention as promising QSL candidates [13,14], in which rare-earth ions form a two-dimensional frustrated triangular lattice regardless of the various crystallization space groups, e.g., $R\bar{3}m$ in AYbSe₂ (A = Na, K, Rb) [6], and $P6_3/mmc$ in CsYbSe₂, etc. [15]. Moreover, LiYbSe₂, a most recently discovered new member of the rare-earth dichalcogenide family, crystallizes in space group $Fd\bar{3}m$, where Yb³⁺ ions arrange into corner-sharing tetrahedra and extend to a three-dimensional (3D) frustrated pyrochlore sublattice [16]. From Dissanayaka Mudiyanse-lage's result in Ref. [16], LiYbSe₂ shows antiferromagnetic interaction at low temperature; however, no long-range magnetic order was detected even down to 70 mK. Thus, LiYbSe₂ provides a rare example of a 3D frustrated magnet with pyrochlore structure in the $AReCh_2$ family and shows sign of realizing intrinsic QSL.

As the energy levels split by the CEF in rare-earth ions are generally comparable to optical phonons or other collective excitations in solids ($1\text{ cm}^{-1} < E < 4000\text{ cm}^{-1}$), Raman scattering has been one useful technique to investigate CEF excitation. It offers great advantages due to the flexibility in studying symmetry selection rules, integrating magnetic field or cryostat, and detecting weak signals even for microcrystallinity, and also the ease of distinguishing its interaction with vibration phonon [11]. There are some

*mzhang@ahu.edu.cn

†zryang@issp.ac.cn

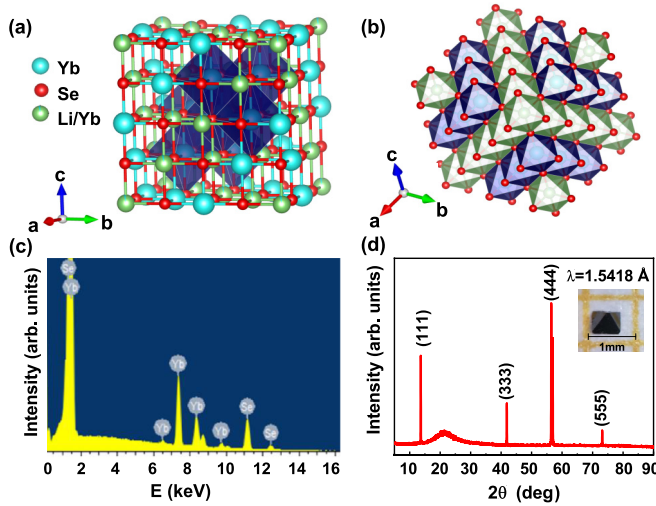


FIG. 1. Structure and characterizations of the LiYbSe₂ single crystal. (a) Unit cell of LiYbSe₂. (b) YbSe₆ and LiSe₆ octahedra arrangement along the [111] direction. (c) The EDS and (d) XRD pattern of LiYbSe₂ single crystal. The inset in (d) is the optical image of one typical piece of the LiYbSe₂ sample.

instances, such as CeAl₂ [17,18], Ce₂O₃ [19], Yb₂O₃ [20], and Tb₂Ti₂O₇ [21]. In this paper, Raman active optical phonons and CEF excitation modes were identified by Raman scattering measurements. This study enriches our knowledge of LiYbSe₂, especially its elementary excitation; the observed CEF-phonon coupling provides the possibility of dressing or investigating the ground state by optical phonon means.

II. EXPERIMENTAL AND CALCULATION METHODS

LiYbSe₂ single crystals were synthesized by the LiCl flux method. A molar ratio of Yb : Se : LiCl = 1 : 3 : 30 was mixed and covered by quartz wool within an alumina crucible, which was then sealed into an evacuated quartz tube. The quartz tube was heated to 400 °C and held for 3 h, then to 850 °C and held for 5 d, and then cooled to room temperature with a rate of 5 °C/h. Octahedral crystals of LiYbSe₂ were obtained after washing with distilled water, as shown in the inset of Fig. 1(d). The nonmagnetic reference compound LiLuSe₂ was synthesized using a similar procedure. As shown in Fig. 1(c), the energy dispersive spectroscopy (EDS) results show the chemical composition value of Yb:Se as ~1:2 while Li was undetected due to it being below the threshold detection limit [22]. The structure of the crystals was identified by x-ray diffraction (XRD) using a Rigaku diffractometer with Cu K α radiation. In Fig. 1(d), the XRD pattern shows strong (*nnn*) peaks, indicating the perfect crystallization of the octahedral plane perpendicular to the [111] axis.

Raman spectra were measured using 633 and 532 nm lasers on a confocal Raman spectrometer (Renishaw inVia) equipped with a closed-cycle cryostat. The incident light was focused on the octahedron surface of the (111) plane by a 20 \times objective lens and the backscattered Rayleigh light was suppressed via a notch filter. The probe spot is ~10 μ m and spectral resolution is ~1 cm⁻¹ with a 2400 l/mm

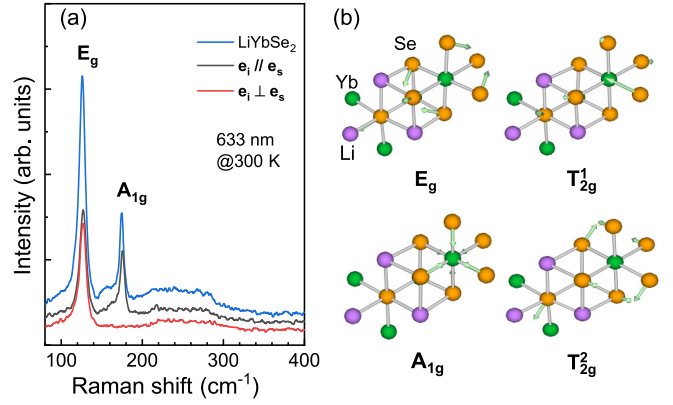


FIG. 2. (a) Polarization-resolved Raman spectra in LiYbSe₂ single crystal at room temperature. (b) Top view along the [111] axis of the eigenvector displacements of Raman active phonon modes in LiYbSe₂.

grating. The laser power was kept below 0.5 mW to avoid damage to samples and to assure negligible local heating. Polarization-resolved Raman spectroscopy was collected by rotating the sample direction or the wave plates; see the schematic illustration in the Supplemental Material (SM), Fig. S1 [23]. We performed the nonmagnetic density functional theory (DFT) calculations with the Yb_3 potentials in which the Yb's 4*f* electrons are frozen in the core. The generalized gradient approximation (Perdew-Burke-Ernzerhof exchange functional) and projector augmented wave method were used, implemented in the Vienna *ab initio* simulation package (VASP) code [24–26]. The experimental lattice constants were used after the atom positions were optimized with the residual Hellmann-Feynman less than 0.001 eV/Å [16]. The plane-wave cutoff energy is 350 eV and the *k* mesh is 9 \times 9 \times 9 in all the calculations. The zone-center phonon modes were calculated with the assistance of the PHONOPY code [27].

III. RESULTS AND DISCUSSION

A. Polarization-resolved Raman scattering at room temperature

LiYbSe₂ crystallizes in the cubic pyrochlore structure with space group *Fd* $\bar{3}$ *m* (No. 227) and the point group *O_h*. As shown in Figs. 1(a) and 1(b), Yb³⁺ and Li⁺ occupy the center of the edge-sharing YbSe₆ and LiSe₆ octahedra [16]. From group theory, the irreducible representations of optical phonon modes for LiYbSe₂ are [28,29]

$$\Gamma = A_{1g} \oplus 4A_{2u} \oplus 4E_u \oplus E_g \oplus 4T_{2u} \oplus 2T_{2g} \oplus 7T_{1u} \oplus T_{1g}, \quad (1)$$

where Raman active phonon modes correspond to nondegenerate *A*_{1*g*} symmetry modes, doubly degenerate *E*_{*g*} symmetry modes, and threefold degenerate *T*_{*2g*} symmetry modes, while *T*_{*1u*} are the infrared active modes; *A*_{*2u*}, *E*_{*u*}, and *T*_{*2u*} are hyper-Raman-active modes. We measured polarization-resolved Raman scattering in both parallel ($\vec{e}_i // \vec{e}_s$) and cross ($\vec{e}_i \perp \vec{e}_s$) polarization configurations with the incident light propagating along the [111] axis at room temperature. As shown in Fig. 2(a), there are two obvious peaks in the

TABLE I. Intensity of the Raman active modes for backscattering from the (111) surface in the O_h point group of LiYbSe₂.

Mode	$\vec{e}_i // \vec{e}_s$	$\vec{e}_i \perp \vec{e}_s$	$\sigma \pm \sigma \pm$	$\sigma \pm \sigma \mp$
A_{1g}	a^2	0	a^2	0
E_g	b^2	b^2	0	b^2
T_{2g}	d^2	$\frac{2}{3}d^2$	$\frac{1}{3}d^2$	$\frac{4}{3}d^2$

parallel configuration near 126.5 and 174.7 cm⁻¹, respectively. In the cross configuration, only Raman peaks near 126.5 cm⁻¹ were detected with the intensity the same as that in the parallel configuration. Angle-dependent Raman spectra indicated that all peaks show circular polarization, as shown in Fig. S5 [23].

To clarify the experimental Raman modes, angle-dependent Raman intensities were calculated based on

$$I \propto |\mathbf{e}_s^\dagger \cdot \mathbf{U}^\dagger \cdot \tilde{\mathbf{R}} \cdot \mathbf{U} \cdot \mathbf{e}_i|^2, \quad (2)$$

where \mathbf{e}_s and \mathbf{e}_i are the polarization vectors of the scattered and incident light, $\tilde{\mathbf{R}}$ is the Raman tensor, and \mathbf{U} is the matrix transforming the crystal coordinates to the laboratory coordinates because the light propagates along the [111] axis [30,31]. In Table I we summarize the phonon intensity in different configurations (see the SM for detailed calculations [23]). E_g mode has the same intensity in both configurations, T_{2g} mode has different intensities in parallel and cross configuration, and A_{1g} modes disappear in cross configuration. Consequently, the Raman peaks at 126.5, and 174.7 cm⁻¹ are then assigned as the E_g and A_{1g} modes, respectively. In addition, our first-principles calculations give four Raman active phonon modes of E_g , T_{2g}^1 , T_{2g}^2 , and A_{1g} with Raman frequencies at 133.38, 135.61, 173.37, and 172.8 cm⁻¹, respectively. Hence, the experimentally observed E_g and A_{1g} modes are close to the theoretical values. The other two T_{2g} modes are too weak to be observed at room temperature. From the following low-temperature Raman results in Fig. 3, T_{2g}^1 and T_{2g}^2 are detected at 153.2 and 163.1 cm⁻¹ at 6 K, respectively. The eigenvector displacements of Raman active phonon modes are shown in Fig. 2(b); all modes involve only the vibrations of Se atoms in the YbSe₆ octahedra. Among this, A_{1g} belongs to one stretching mode with threefold rotating symmetry and is nondegenerate as Se atoms vibrate along the threefold axis; meanwhile E_g and T_{2g} originate from shearing vibration of Se atoms and doubly degenerate vibration can be clearly seen from Fig. 2(b) for the E_g mode.

B. Temperature-dependent Raman scattering

Figure 3 shows the temperature-dependent Raman spectra of LiYbSe₂ single crystal in the range 6–300 K. With temperature decreasing, there are some remarkable features; e.g., (i) at first glance, the E_g mode shifts to a lower energy of 116.2 cm⁻¹ at 6 K, which actually involves the CEF1 mode and the E_g mode mixed as discussed below, and its intensity shows immense enhancement; (ii) as marked by the asterisks in Fig. 3(a), some broad peaks are negligible at room temperature and develop with cooling, particularly the peaks

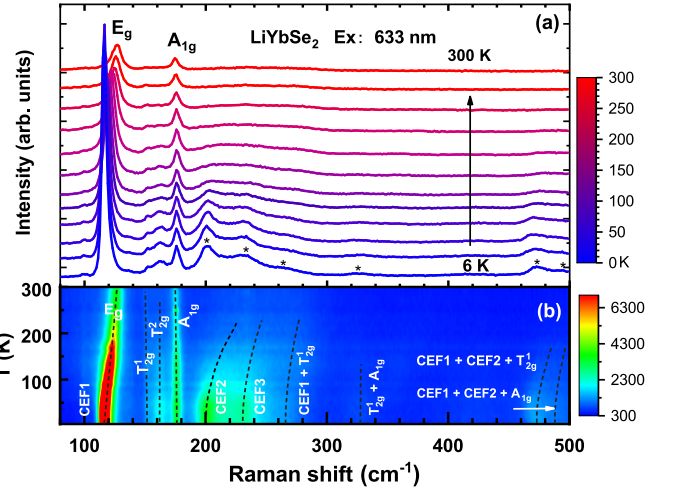


FIG. 3. (a) Temperature-dependent Raman spectra for LiYbSe₂ single crystal at selected temperature. The asterisks mark the broad peaks rising at low temperature. All plots are evenly spaced in a linear scale for clarity. (b) Contour plots of the temperature-dependent Raman intensity from 6 to 300 K. The black dashed lines are the guidelines for the Raman frequencies shift.

near 200.9, 232.1, and 472.2 cm⁻¹ at 6 K; (iii) all the above peaks simultaneously soften with decreasing temperature, as indicated in Fig. 3(b).

For further analysis, nonmagnetic references of LiLuSe₂ were also grown and the temperature-dependent Raman spectra were measured to compare. As shown in Fig. 4, it is obvious that all the above features are absent in LiLuSe₂. These remind us that the abnormal peaks in LiYbSe₂ are related to the magnetic ions Yb³⁺, which potentially originate from the electronic transitions between the CEF-split energy levels. In LiYbSe₂, Yb³⁺ 4f¹³ orbitals show an electronic ground state of total angular momentum $J = 7/2$ with

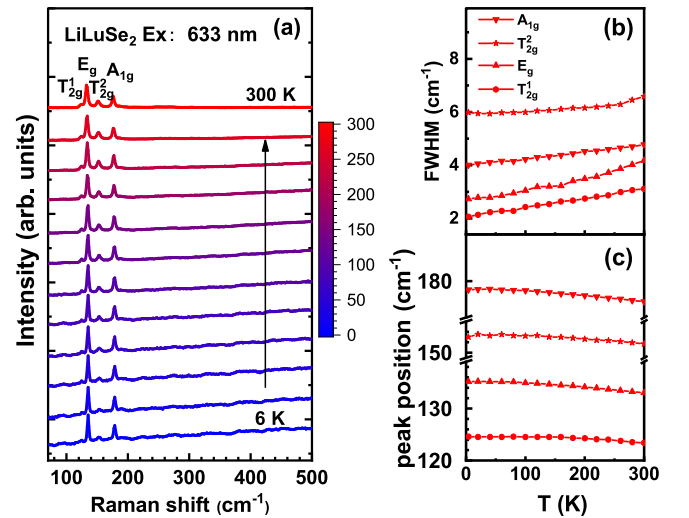


FIG. 4. (a) Temperature-dependent Raman spectra for the non-magnetic reference of LiLuSe₂ single crystal. All plots are evenly spaced in a linear scale for clarity. (b), (c) The FWHM and peak position of Raman modes vs temperature in LiLuSe₂.

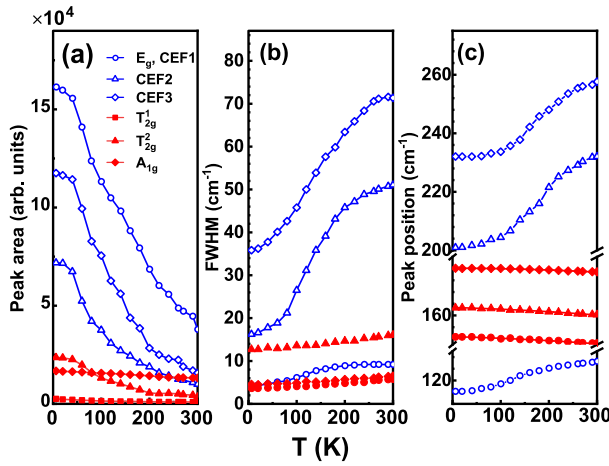


FIG. 5. Experimental results for the temperature dependence of the peak area, FWHM, and position of the main Raman modes. The red corresponds to the bare phonon modes, and the blue corresponds to the CEF modes.

$2J + 1 = 8$ -fold degeneracy, and the YbSe_6 octahedron has the same point group symmetry of D_{3d} as CsYbSe_2 , NaYbSe_2 , and $\text{Yb}_2\text{Ti}_2\text{O}_7$, which lifts the degeneracy of Yb^{3+} ions to four Kramers doublets [31–33]. Thus, we assigned the three abnormal modes at 116.2, 200.9, and 232.1 cm^{-1} of 6 K to CEF1, CEF2, and CEF3, respectively, which is comparable to that of CsYbSe_2 [31] and NaYbSe_2 [32]. It is worth mentioning that vibration mode E_g merges into the strong CEF1 mode due to their close energy levels; hence we use the labels (E_g , CEF1) in the figures. We also calculated the CEF levels using the point charge model with PYCRYSTALFIELD software [34]. The calculated CEF levels are 11.7, 12.4, and 29.6 meV ($= 94.8, 99.9, \text{ and } 238.6 \text{ cm}^{-1}$), respectively, which are approximate to the experimental values except for the second one. The other peaks with higher wave numbers are higher-order modes stimulated by the resonant excitation as discussed below.

Actually, the strong temperature dependence of intensity and linewidth of the Raman peaks is a characteristic quality of the electronic transition [35]. Because the electron populations of the ground state increase with decreasing temperature, the spectral weights of these features increase dramatically [20,35]. Therefore, CEF excitations are nearly negligible at room temperature due to their weakness and broad linewidth; this is conducive to distinguishing the CEF excitation mode and the phonon mode through the temperature dependence of the Raman spectra. We fitted the Raman spectra with several Lorentzian shapes to obtain the peak evolution (see the fitting results in Fig. S2 [23]); as shown in Figs. 5(a) and 5(b), the peak area and full width at half maximum (FWHM) of the CEF excitation modes exhibit stronger temperature dependence than that of phonons. With decreasing temperature, all pure phonon modes can be well fitted by a four-phonon anharmonic approximation model for the linewidth narrowing and the peak position stiffening; however, all CEF modes show unusual enormous narrowing and distinctive redshift [see Figs. 5(b) and 5(c), and Figs. S3 and S4] [23,36,37]. Moreover, the E_g peak hidden in the (E_g , CEF1) profile also

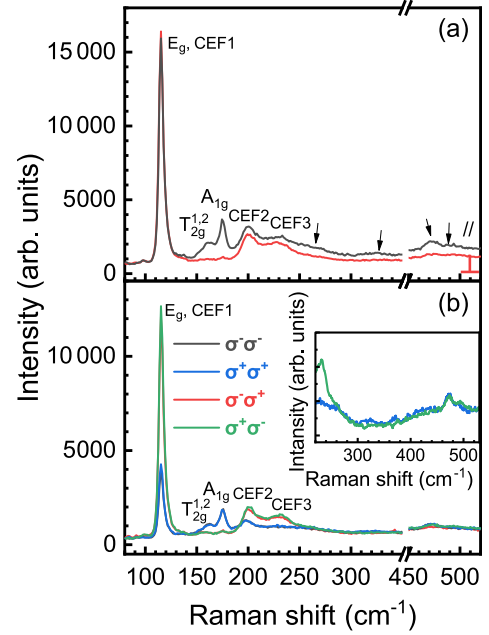


FIG. 6. Polarization-resolved Raman spectra of LiYbSe_2 with (a) linearly polarized and (b) circularly polarized light at 6 K. The inset in (b) is the enlarged view for the combination modes at high wave numbers.

exhibits softening in contrast to other phonons; this can be interpreted by its coupling to CEF1 due to the close energy between E_g and CEF1. In other words, there is energy exchange between E_g and CEF1. Analogous phonon shifts were also reported in CsYbSe_2 [31], NaYbSe_2 [32], and CeCu_2 [38].

As mentioned above, the CEF excitations shift unusually to lower energy with decreasing temperature; we notice that similar phenomena have been observed in NaYbSe_2 , where the temperature-affected electronegativity plays a critical role in the abnormal redshift [32]. When temperature decreases, the lattice shrinks and the overlap of electron clouds between Yb and Se enhances; accordingly the electronegativity of Se decreases and then gives lower CEF levels. In consideration of similar YbSe_6 octahedron coordination, we believe this electronegativity effect is also at work in LiYbSe_2 , where the reduction of the effective charges of the Se weakens the CEF strength and leads to a lower CEF level with cooling. In addition, CEF-phonon coupling seemingly attenuates this redshift feature for (E_g , CEF1), as shown in Fig. 5(c).

C. Polarization-resolved Raman spectra at low temperature

We then measured the polarization-resolved Raman spectra by linearly polarized and left- (right-) handed polarized σ^+ (σ^-) light at 6 K by rotating the wave plates. The σ^\pm light can be represented by Jones vectors, $\sigma^\pm = \frac{1}{\sqrt{2}}(\pm i)$; then the phonon mode intensities were calculated (see the SM [23]) and are listed in Table I. Figure 6(a) show the linear polarization-resolved Raman spectra; all pure CEF modes share similar polarization profiles with the E_g mode, suggesting that CEF modes share forms of Raman tensors that are to similar E_g phonon modes. However, T_{2g} modes were extinctive

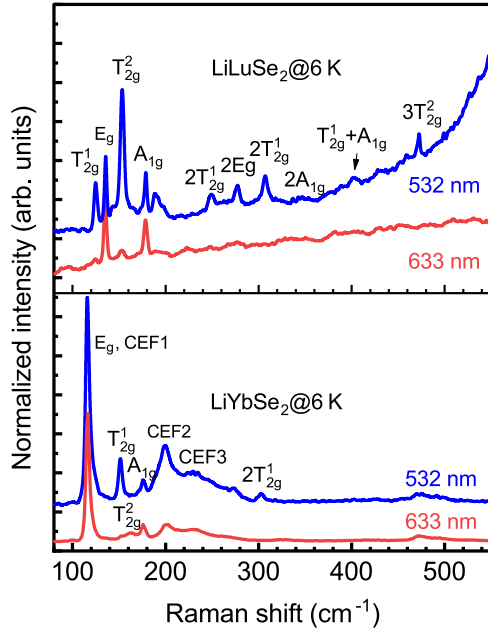


FIG. 7. Raman spectra of LiYbSe₂ and LiLuSe₂ with different excitation wavelengths. The Raman intensities are normalized by that of the A_{1g} modes.

in cross configuration just like A_{1g}, which is inconsistent with the selection rule (see Table I). Similar phenomena were also detected in LiLuSe₂, as shown in Fig. S7 [23]. This can be interpreted as a breakdown of the selection rule which is quite common under resonant excitations [11]. In practice, LiYbSe₂ and LiLuSe₂ single crystals are dark red in color, and the LiLuSe₂ single crystal shows a band gap of ~2.0 eV according to the photoluminescence spectrum excited by 532 nm (see Fig. S8 [23]). Thus, the 633 nm (1.96 eV) and 532 nm (2.33 eV) light are around the resonant-excitation condition, which can be further evidenced by the excitation wavelength dependent Raman intensities of T_{2g} as indicated in Fig. 7. This lies in excellent agreement with the observation of higher-order modes in LiYbSe₂ and LiLuSe₂ (see Fig. 7), which are generally weak unless the resonant-excitation condition satisfied then strongly enhances the scattering rate.

For circularly polarized Raman spectra as shown in Fig. 6(b), T_{2g} shares a similar helicity-conserved feature with A_{1g} ($\sigma i \sigma s = \sigma \pm \sigma \pm$), which is consistent with the calculations in Table I and the breakdown of the selection rule discussed above. The E_g mode should be helicity changed ($\sigma i \sigma s = \sigma \pm \sigma \mp$) with zero intensity in the cocircular polarization configuration; moreover, CEF1–CEF3 appear in both configuration and exhibit more strongly in the cross-circular polarization. The modes at 265.1, 472.2, and 491.1 cm⁻¹ show up in both configurations, which are more like CEF modes and then assigned as CEF1 + T_{2g}¹, CEF1 + CEF2 + T_{2g}¹, and CEF1 + CEF2 + A_{1g}, respectively, according to their energy. These modes show coincident redshifts at low temperature just like CEF modes. The mode at 328.6 cm⁻¹ was insensitive to temperature as shown in Fig. 3(b), which should come from pure phonons similarly, with the usual faint blueshift of higher-order modes in LiLuSe₂ (see Fig. S9 [23]); the possible assignment is T_{2g}¹ + A_{1g} or 2T_{2g}². We list all Raman modes

TABLE II. Summary of assignment of experimental modes and theoretical modes.

Experimental wave number (cm ⁻¹) (6 K)	Experimental wave number (cm ⁻¹) (300 K)	Theoretical wave number (cm ⁻¹)	Assignment
116.2	126.5	133.38	E _g , CEF1
152.7	150.5	135.61	T _{2g} ¹
162.6	160.4	173.37	T _{2g} ²
176.1	174.7	172.8	A _{1g}
200.9	232.1		CEF2
232.1	257.6		CEF3
265.1	273.6		CEF1 + T _{2g} ¹
328.6			T _{2g} ¹ + A _{1g} , 2T _{2g} ²
472.2	501.8		CEF1 + CEF2 + T _{2g} ¹
491.1	514.2		CEF1 + CEF2 + A _{1g}

and the combination modes according to their energy and temperature dependence in Table II.

Photons can carry angular momentum, e.g., the $\sigma+$ ($\sigma-$) photon carries angular momentum of $+\hbar$ ($-\hbar$). For Raman modes excited by circularly polarized light, the helicity of scattered light can be changed ($\sigma i \sigma s = \sigma \pm \sigma \mp$, corresponding to $J \pm J \pm$ acting on the system and the system obtains angular momentum of $\pm 2\hbar$) or conserved ($\sigma i \sigma s = \sigma \pm \sigma \pm$, corresponding to $J \mp J \pm$ acting on the system and the system obtains angular momentum of $0\hbar$) depending on the selection rule. Circularly polarized Raman spectra can provide information about the Kramers eigenstates by angular momentum conservation. The ground state spin-orbit manifold $J = 7/2$ splits into four Kramers pairs $|\psi_{0,1,2,3}^{\pm}\rangle$, of which the total angular momentum in the system can take values of $\pm 1/2$, $\pm 3/2$, $\pm 5/2$, and $\pm 7/2$. The calculated CEF parameters and Kramers eigenstates can be found in the SM [23]; the ground states of these models are $|\psi_0^{\pm}\rangle = \pm 0.516|\frac{7}{2}, \mp \frac{1}{2}\rangle - 0.804|\frac{7}{2}, \pm \frac{5}{2}\rangle + 0.295|\frac{7}{2}, \mp \frac{7}{2}\rangle$, and CEF1, CEF2, and CEF3 describe the transition between the excited doublets and the ground state $|\psi_0^{\pm}\rangle$. The selection rule for helicity-resolved CEF modes can be accounted for using the conservation law of angular momentum as follows [39]:

$$\Delta J = \sigma_i - \sigma_s + Np, \quad (3)$$

where ΔJ represents the angular momentum variation between the excited state and the ground state, σ is the helicity of the light, N is the rotational symmetry of the system, and p is an arbitrary integer. Because the direction of the light propagation is along the [111] axis, thus $N = 3$ for LiYbSe₂ due to its point group of O_h . Then for the cross-circular polarization configuration, $\Delta J = \pm 2\hbar, \mp \hbar$; for cocircular polarization configuration, $\Delta J = 0, \pm 3\hbar$. Based on the Kramers eigenstates shown in Table SI [23], it is allowed to appear in both the cross-circular and cocircular polarization configurations for CEF2 and CEF3. Therefore, the single angular momentum eigenstate calculated for the second CEF level is impossible combining with experimental results;

a more precise model or other experiment, e.g., inelastic neutron scattering, is necessary for eigenstate calculations.

IV. CONCLUSIONS

In summary, by combining the polarization-resolved Raman spectra, temperature-dependent Raman spectra, and theoretical calculations, we identified four Raman active phonon modes, three CEF excitation modes, and higher-order Raman modes contributed by the resonant excitation with 633 and 532 nm light in LiYbSe₂. Helicity-resolved Raman spectra show that CEF modes appear in both cross-circular and cocircular polarization, which excluded the single angular momentum eigenstate predicted from the point charge model. CEF excitations exhibit an unusual redshift with decreasing temperatures due to the reduction of Se atom electronegativity, and weak CEF-phonon coupling was supposed due to the close energy between CEF1 excitation and the E_g mode. The above results help to clarify the interaction between phonons and electrons and widen the way to study 3D frustration magnets or novel QSL states in LiYbSe₂; meanwhile, the Raman

scattering has been proven to be a powerful tool for relevant studies in this system.

ACKNOWLEDGMENTS

We are grateful for financial support from the National Key Research and Development Program of China (Grant No. 2022YFA1602603), the Natural Science Foundation of Anhui Province (Grants No. 2308085QA18 and No. 2308085MA16), the Key Project of Natural Scientific Research of Universities in Anhui Province (Grants No. KJ2021A0064 and No. KJ2021A0068), and the National Natural Science Foundation of China (Grants No. 12374049, No. 12004004, and No. 12204004). This work was supported by the Basic Research Program of the Chinese Academy of Sciences Based on Major Scientific Infrastructures (Grant No. JZHKYPT-2021-08). Yonghui Zhou was supported by the Youth Innovation Promotion Association CAS (Grant No. 2020443). The numerical calculations in this paper have been done on the computing facilities in the High-Performance Computing Center (HPCC) of Nanjing University.

-
- [1] L. Balents, Spin liquids in frustrated magnets, *Nature (London)* **464**, 199 (2010).
- [2] J. G. Rau and M. J. P. Gingras, Frustrated quantum rare-earth pyrochlores, *Annu. Rev. Condens. Matter Phys.* **10**, 357 (2019).
- [3] L. Savary and L. Balents, Quantum spin liquids: A review, *Rep. Prog. Phys.* **80**, 016502 (2017).
- [4] C. Broholm, R. J. Cava, S. A. Kivelson, D. G. Nocera, M. R. Norman, and T. Senthil, Quantum spin liquids, *Science* **367**, eaay0668 (2020).
- [5] Y. Zhou, K. Kanoda, and T.-K. Ng, Quantum spin liquid states, *Rev. Mod. Phys.* **89**, 025003 (2017).
- [6] W. W. Liu, Z. Zhang, J. T. Ji, Y. X. Liu, J. Q. Li, X. Q. Wang, H. C. Lei, G. Chen, and Q. M. Zhang, Rare-earth chalcogenides: A large family of triangular lattice spin liquid candidates, *Chin. Phys. Lett.* **35**, 117501 (2018).
- [7] Y. Li, G. Chen, W. Tong, L. Pi, J. Liu, Z. Yang, X. Wang, and Q. Zhang, Rare-earth triangular lattice spin liquid: A single-crystal study of YbMgGaO₄, *Phys. Rev. Lett.* **115**, 167203 (2015).
- [8] S. Gao, F. Xiao, K. Kamazawa, K. Ikeuchi, D. Biner, K. W. Krämer, C. Rüegg, and T.-h. Arima, Crystal electric field excitations in the quantum spin liquid candidate NaErS₂, *Phys. Rev. B* **102**, 024424 (2020).
- [9] Y. D. Li, X. Q. Wang, and G. Chen, Anisotropic spin model of strong spin-orbit-coupled triangular antiferromagnets, *Phys. Rev. B* **94**, 035107 (2016).
- [10] J. A. M. Paddison, M. Daum, Z. Dun, G. Ehlers, Y. Liu, Matthew B. Stone, H. Zhou, and M. Mourigal, Continuous excitations of the triangular-lattice quantum spin liquid YbMgGaO₄, *Nat. Phys.* **13**, 117 (2016).
- [11] G. Schaack, in *Light Scattering in Solids VII: Crystal-Field and Magnetic Excitations*, edited by M. Cardona and G. Güntherodt (Springer, Berlin, 2000), p. 24.
- [12] P. Thalmeier, Dual model for magnetic excitations and superconductivity in UPd₂Al₃, *Eur. Phys. J. B* **27**, 29 (2002).
- [13] A. O. Scheie, E. A. Ghioldi, J. Xing, J. A. M. Paddison, N. E. Sherman, M. Dupont, L. D. Sanjeeva, S. Lee, A. J. Woods, D. Abernathy, D. M. Pajerowski, T. J. Williams, S. S. Zhang, L. O. Manuel, A. E. Trumper, C. D. Pemmaraju, A. S. Sefat, D. S. Parker, T. P. Devereaux, R. Movshovich *et al.*, Proximate spin liquid and fractionalization in the triangular antiferromagnet KYbSe, *Nat. Phys.* **20**, 74 (2024).
- [14] P.-L. Dai, G. Zhang, Y. Xie, C. Duan, Y. Gao, Z. Zhu, E. Feng, Z. Tao, C.-L. Huang, H. Cao, A. Podlesnyak, G. E. Granroth, M. S. Everett, J. C. Neuefeind, D. Voneshen, S. Wang, G. Tan, E. Morosan, X. Wang, H.-Q. Lin *et al.*, Spinon Fermi surface spin liquid in a triangular lattice antiferromagnet NaYbSe₂, *Phys. Rev. X* **11**, 021044 (2021).
- [15] J. Xing, L. D. Sanjeeva, J. Kim, G. R. Stewart, M.-H. Du, F. A. Reboledo, R. Custelcean, and A. S. Sefat, Crystal synthesis and frustrated magnetism in triangular lattice CsRESe₂ (RE = La – Lu): Quantum spin liquid candidates CsCeSe₂ and CsYbSe₂, *ACS Mater. Lett.* **2**, 71 (2019).
- [16] R. S. Dissanayaka Mudiyanse, H. Wang, O. Vilella, M. Mourigal, G. Kotliar, and W. Xie, LiYbSe₂: Frustrated magnetism in the pyrochlore lattice, *J. Am. Chem. Soc.* **144**, 11933 (2022).
- [17] P. Thalmeier and P. Fulde, Bound state between a crystal-field excitation and a phonon in CeAl₂, *Phys. Rev. Lett.* **49**, 1588 (1982).
- [18] G. Güntherodt, A. Jayaraman, G. Batlogg, M. Croft, and E. Melczer, Raman scattering from coupled phonon and electronic crystal-field excitations in CeAl₂, *Phys. Rev. Lett.* **51**, 2330 (1983).
- [19] A. Sethi, J. E. Slimak, T. Kolodiazny, and S. L. Cooper, Emergent vibronic excitations in the magnetodielectric regime of Ce₂O₃, *Phys. Rev. Lett.* **122**, 177601 (2019).
- [20] J. E. Slimak, A. Cote, G. J. MacDougall, and S. L. Cooper, Soft-phonon anomalies and crystal electric field–phonon coupling in

- cubic lanthanide sesquioxides Eu_2O_3 and Yb_2O_3 , *Phys. Rev. B* **108**, 045128 (2023).
- [21] M. Mączka, M. L. Sanjuán, A. F. Fuentes, K. Hermanowicz, and J. Hanuza, Temperature-dependent Raman study of the spin-liquid pyrochlore $\text{Tb}_2\text{Ti}_2\text{O}_7$, *Phys. Rev. B* **78**, 134420 (2008).
- [22] J. P. Cotter, and J. C. Fitzmaurice, and I. P. Parkin, New routes to alkali-metal-rare-earth-metal sulfides, *J. Mater. Chem.* **4**, 1603 (1994).
- [23] See Supplemental Material at <http://link.aps.org/supplemental/10.1103/PhysRevB.109.174101> for details on analysis of phonon symmetry with group theory, point charge model calculations, Lorentzian fitting of the Raman spectra, anharmonic model fitting of temperature evolutions of phonon modes, angle-dependent polarized Raman spectra, nonmagnetic-reference sample LiLuSe_2 , and calculated phonon dispersion. It also contains Refs. [28,31–34,37,40].
- [24] G. Kresse and J. Hafner, *Ab initio* molecular dynamics for liquid metals, *Phys. Rev. B* **47**, 558 (1993).
- [25] G. Kresse and J. Furthmüller, Efficient iterative schemes for *ab initio* total-energy calculations using a plane-wave basis set, *Phys. Rev. B* **54**, 11169 (1996).
- [26] J. P. Perdew, K. Burke, and M. Ernzerhof, Generalized gradient approximation made simple, *Phys. Rev. Lett.* **77**, 3865 (1996).
- [27] A. Togo and I. Tanaka, First principles phonon calculations in materials science, *Scr. Mater.* **108**, 1 (2015).
- [28] M. I. Aroyo, A. Kirov, C. Capillas, J. M. Perez-Mato, and H. Wondratschek, Bilbao Crystallographic Server. II. Representations of crystallographic point groups and space groups, *Acta Crystallogr., Sect. A: Found. Crystallogr.* **62**, 115 (2006).
- [29] L. Elcoro, B. Bradlyn, Z. Wang, M. G. Vergniory, J. Cano, C. Felser, B. A. Bernevig, D. Orobengoa, G. de la Flor, and M. I. Aroyo, Double crystallographic groups and their representations on the Bilbao Crystallographic Server, *J. Appl. Crystallogr.* **50**, 1457 (2017).
- [30] X. Lu, M. I. B. Utama, J. Zhang, Y. Zhao, and Q. Xiong, Layer-by-layer thinning of MoS_2 by thermal annealing, *Nanoscale* **5**, 8904 (2013).
- [31] Y. Y. Pai, C. E. Marvinney, L. B. Liang, J. Xing, A. Scheie, A. A. Purezky, G. B. Halasz, X. Li, R. Juneja, A. S. Sefat, D. Parker, L. Lindsay, and B. J. Lawrie, Mesoscale interplay between phonons and crystal electric field excitations in quantum spin liquid candidate CsYbSe_2 , *J. Mater. Chem. C* **10**, 4148 (2022).
- [32] Z. Zhang, X. L. Ma, J. S. Li, G. H. Wang, D. T. Adroja, T. P. Perring, W. W. Liu, F. Jin, J. T. Ji, Y. M. Wang, Y. Kamiya, X. Q. Wang, J. Ma, and Q. M. Zhang, Crystalline electric field excitations in the quantum spin liquid candidate NaYbSe_2 , *Phys. Rev. B* **103**, 035144 (2021).
- [33] J. Gaudet, D. D. Maharaj, G. Sala, E. Kermarrec, K. A. Ross, H. A. Dabkowska, A. I. Kolesnikov, G. E. Granroth, and B. D. Gaulin, Neutron spectroscopic study of crystalline electric field excitations in stoichiometric and lightly stuffed $\text{Yb}_2\text{Ti}_2\text{O}_7$, *Phys. Rev. B* **92**, 134420 (2015).
- [34] A. Scheie, PYCRYSTALFIELD: Software for calculation, analysis and fitting of crystal electric field Hamiltonians, *J. Appl. Crystallogr.* **54**, 356 (2021).
- [35] G. Schaack, Raman scattering by crystal-field excitations, in *Light Scattering in Solids VII* (Springer, Berlin, 2000), p. 24.
- [36] M. Balkanski, R. F. Wallis, and E. Haro, Anharmonic effects in light scattering due to optical phonons in silicon, *Phys. Rev. B* **28**, 1928 (1983).
- [37] H. Tang and I. P. Herman, Raman microprobe scattering of solid silicon and germanium at the melting temperature, *Phys. Rev. B* **43**, 2299 (1991).
- [38] M. Loewenhaupt and U. Witte, Coupling between electronic and lattice degrees of freedom in $4f$ -electron systems investigated by inelastic neutron scattering, *J. Phys.: Condens. Matter* **15**, S519 (2003).
- [39] Y. Tatsumi, T. Kaneko, and R. Saito, Conservation law of angular momentum in helicity-dependent Raman and Rayleigh scattering, *Phys. Rev. B* **97**, 195444 (2018).
- [40] I. Yasuda, T. Kawada, H. Matsumoto, M. Kawaguchi, and M. Hayashi, Helicity-resolved Raman spectroscopy of mono- and a few-layers-thick PtSe_2 , *Appl. Phys. Express* **16**, 053005 (2023).